

Referee #1

Dear Reviewer,

We would like to thank you for your supporting and constructive comments. We here provide some discussion on your specific comments. We fully addressed these comments (as well as your technical corrections) within the revised version of our manuscript (See supplement).

Specific Comment (SC)#1

Page 2511; line 1. "The lack of specific current-meter measurements does not allow for a realistic determination of vorticity and, in particular, for a validation of our model".

I understand that measurements do not allow the determination of vorticity but you have model data to validate your results. This should not be difficult to do and would be a good test for your theoretical estimates. I do not necessarily expect a perfect matching between model and theory, but such comparison is of interest and would be an added value of the paper.

We absolutely agree with the reviewer and, in the past, we tried to figure out how to make use of numerical outputs in order to validate (or just compare) our analytic/ experimental results with numerical ones. From several discussions we had with our colleagues (numerical ocean modelers) it came out that the calculations of vorticity field (i.e., the vertical vorticity ζ) from the horizontal velocity components provided by Mediterranean Sea numerical models is not trivial. Such a calculation may result to be meaningless, due to grid problems (Dr. G. Sannino, personal communication, 2015; Dr. L. Palatella, personal communication, 2015): i) numerical outputs are provided on staggered-grids and it would be quite hard to retrieve the original non-staggered grid information; ii) spatial resolutions are too coarse and, in particular, bottom velocities are available on a very few cross-stream grid points (one or two at the western sill; See figure below). We are aware of some other ocean models that provide, directly, the vorticity field (and then they obtain the velocity field from those). However, these products are not available on the main web portal for operational oceanography (e.g., MyOcean). In synthesis we believe that to include in this work ad hoc numerical runs that provide the bottom vorticity field for the seasons we investigated (i.e., January 1997 and May 1998) is not feasible. Such a comment provided by the Reviewer can, however, constitute the main objective of a future work.

In the revised manuscript we included this discussion. See line 355-356; 378-382.

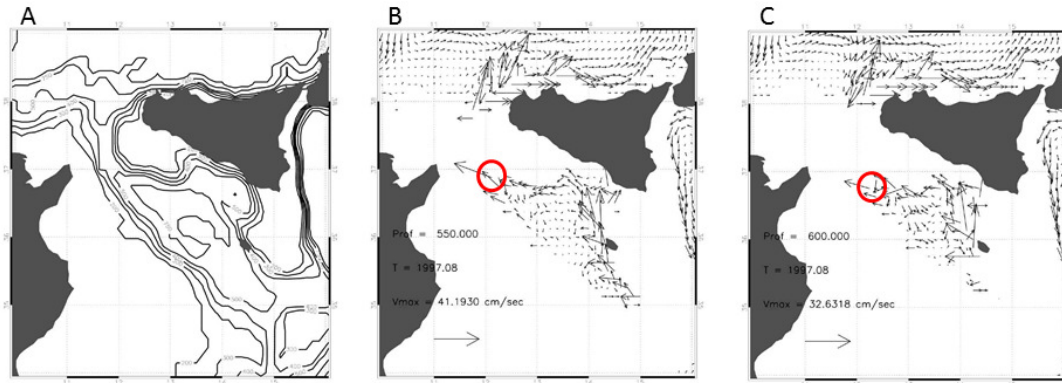


Figure. Monthly mean velocities from PROTHEUS numerical data (January 1997), a relatively coarse resolution Mediterranean model ($1/8^\circ \times 1/8^\circ$) based on the MIT general circulation model (MITgcm; Sannino et al., 2009; Sannino, personal communication). Panel A: Bathymetry used in the model; Panel B: velocity filed at 550 m depth; Panel C: : velocity filed at 600 m depth. The figure show that bottom velocities within the channel (red circles) do not allow to evaluate the vorticity filed due to the coarse horizontal resolution of the model.

SC#2

Page 2512. *I might be missing something important, but I do not understand the analysis included herein. Why is not $\varepsilon = 0$ (eq. 19) if the terms $\varepsilon 1$, $\varepsilon 2$ and $\varepsilon 3$ are derived from the solution to (16a)? Perhaps you used a different friction term in equation 16a (that is, something different to $-K^*\zeta u/h^2$, with $K^* = 2.6 \cdot 10^{-2}$?) Please clarify this.*

Thank you for stressing this point. Equation (14) is from the continuity and vorticity equations; its analytic solution is Equation (15). Independently from this analytic solution of Π (i.e., Eq. 15), we analyze and plot each term of (14) as a function of ζ , which is obtained from (13). All this represents a sort of independent validation of the PV balance since we are not making use of (15). We hope this is now clearer and we accordingly improved the text of our manuscript in the revised version. See line 416-418

SC#3

Page 2514; line 4-6. *“Knowledge of the downstream evolution of ζ allowed us (i) to infer the deep vein dynamics, in particular, around the sill region, where the*

flow is dramatically non-geostrophic".

Is the flow around the sill dramatically non-geostrophic? If this was the case you are violating your assumption $\zeta \ll f$. An explanation is required.

Many thanks for noticing that: this sentence needs indeed to be changed. Even at the western sill where the width of the flow is $\sim 2 \times 10^4$ m and velocity ~ 40 cm/s, estimations of relative vorticity ($\sim 2 \times 10^{-5}$) do not exceed the value of planetary vorticity. So we rephrased the sentence as: "...around the sill region, where frictional, entrainment, and stretching effects all play a crucial role". See line 456-461

Friction and mixing effects on potential vorticity for bottom current crossing a marine strait: an application to the Sicily Channel (central Mediterranean Sea)

F. Falcini and E. Salusti

CNR-ISAC, Via del Fosso del Cavaliere 100, 00133 Rome, Italy

Correspondence to: F. Falcini (f.falcini@isac.cnr.it)

Abstract

We discuss here the evolution of vorticity and potential vorticity (PV) for a bottom current crossing a marine channel in shallow-water approximation, focusing on the effect of friction and mixing. The purpose of this research is indeed to investigate the role of friction and vertical entrainment on vorticity and PV spatial evolution in channels or straits when along-channel morphology variations are significant. To pursue this investigation, we set the vorticity and PV equations for a homogeneous bottom water vein and we calculate these two quantities as an integral form. Our theoretical findings are discussed by means of in situ hydrographic data related to the Eastern Mediterranean Deep Water, i.e., a dense, bottom water vein that flows northwestward, along the Sicily Channel (Mediterranean Sea). Indeed, the narrow sill of this channel implies that friction and entrainment need to be considered. Small tidal effects in the Sicily Channel allow for a steady theoretical approach.

We argue that bottom current vorticity is prone to significant sign changes and oscillations due to topographic effects when, in particular, the current flows over the sill of a channel. These vorticity variations are, however, modulated by frictional effects due to seafloor roughness and morphology. Such behavior is also reflected in the PV spatial evolution, which shows an abrupt peak around the sill region. Our diagnoses on vorticity and PV allow us to obtain general insights about the effect of mixing and friction on the pathway and internal structure of bottom-trapped currents flowing through channels and straits, and to discuss spatial variability of the frictional coefficient. Our approach significantly differs from other PV-constant approaches previously used in studying the dynamics of bottom currents flowing through rotating channels.

1 Introduction

An ongoing debate in [diagnostic models](#) for currents that flow over a sill in a rotating channel with varying cross sections concerns the effect of friction and mixing, which clearly play an important role in the presence of morphological constraints (Pratt et al., 2008; Pratt and Whitehead, 2008). [Despite](#)

37 such a role, these two key effects are often not considered in the literature. Idealized models for
38 marine currents flowing through rotating channels (e.g., Whitehead et al., 1974; Gill, 1977; Borenas
39 and Lundberg, 1986, 1988; Killworth, 1992) usually assume a steady state and are often simplified,
40 out of necessity, for a feasible analytic investigation (Pratt and Whitehead, 2008). This, for instance,
41 leads to friction being neglected, assuming a uniform potential vorticity (PV) and considering channels
42 with rectangular or smooth, idealized cross sections in order to avoid dynamic pathologies at the
43 current lateral edges (Lacombe and Richez, 1982; Hogg, 1983; Pratt et al., 2008).

44 In particular, the most often cited models for these currents assume a zero-potential vorticity
45 flow (Whitehead et al., 1974; Borenas and Lundberg, 1988). Such an assumption is mostly applied for
46 fluid columns coming from a quasi-quiet state and then severely squashed as they
47 cross the sill of a channel. [Along-channel profiles of depth and velocity of these approximated currents](#)
48 [are particularly simple to predict and, for the case of a rectangular cross section](#), it has been
49 demonstrated that such flows are also stable (Paldor, 1983). In fact, realistic bottom marine currents
50 that are confined to channels or straits show a thickness that goes to zero at the lateral edges, which
51 can lead to pathological features in terms of flow stability (Pratt et al., 2008).

52 A second, often adopted approximation is given by disregarding friction and vertical
53 entrainment of bottom currents flowing in rotating channels (Armi and Farmer, 1985; Bryden and
54 Kinder, 1991; Whitehead et al., 1974; Gill, 1977; Borenas and Lundberg, 1986). Friction and
55 entrainment in fact play an important role for currents crossing channels or straits (Johnson and
56 Ohlsen, 1994), in particular when along-channel morphology variations are present (Borenas and
57 Lundberg, 1986, 1988; Killworth, 1992, among others). [Experimental data on this regard have shown](#)
58 [complicated dynamics that suggest a strong effect of both interfacial and bottom friction that may](#)
59 [induce a secondary circulation \(Johnson et al., 1976\)](#).

60 These considerations are at the base of our interest for a more realistic analysis of bottom
61 currents that cross a narrow marine channel, in the presence of an irregular morphology, and flow
62 underneath upper layers that have different dynamics. [We do not aim to provide a prognostic model to](#)
63 [be tested with observations, but rather, to introduce the potential effect of bottom friction and](#)
64 [entrainment effects in integral forms of vorticity and PV](#). To pursue such an investigation, we derive
65 vorticity and PV equations from the classic stream-tube model (Smith, 1975; Killworth, 1977), which
66 describes the steady properties of a homogeneous, [viscous bottom water vein](#), also considering
67 entrainment in the mass conservation equation (Turner, 1986). We then discuss these equations in
68 order to figure out the role of seafloor morphology, friction, and mixing in marine channel dynamics.
69 We finally introduce the hydrographic settings of the Sicily Channel (Fig. 1) (Astraldi et al., 2001; A01
70 hereafter) and employ interpolated, cross-averaged flow velocity (\bar{u}) and thickness (\bar{h}) data related
71 to the Eastern Mediterranean Deep Water (EMDW, a bottom vein flowing northwestward through the

72 Sicily Channel) in order to diagnose our vorticity and PV equations. The EMDW flows underneath the
 73 Levantine Intermediate Water (LIW) and the Modified Atlantic Water (MAW). Those currents constitute
 74 a three layer system (Fig. 2), whose hydrodynamics are strongly affected by baroclinic, mixing, and
 75 topographic effects (A01).

76 Our approach differs from a similar investigation proposed by Hogg (1983) and Whitehead
 77 (1998), among many others, who analyzed the hydraulic control and frictionless flow separation in the
 78 Vema Channel. The Sicily Channel has relatively unimportant tides; its sill is 300 m deep and shows
 79 an irregular and narrow morphology, all features that make this channel particularly suitable for our
 80 goals and theoretical approaches. In particular, the usual inviscid quasi-geostrophic approach does
 81 not seem particularly adequate in the Sicily Channel.

82

83 **2 Momentum and mass conservation of dense flows for realistic channels**

84 Here we consider the dynamics of a shallow, homogeneous, bottom layer of fluid flowing in a deep
 85 channel, underneath upper moving layers of water that have a slightly lower density. The channel is
 86 thought to be aligned along the x direction and has a realistic, quasi-rounded cross section (Fig. 2a).
 87 The stream-wise evolution of such a bottom flow is governed by the shallow-water equations. The use
 88 of the full equations, rather than “balance” equations or other approximations, is required in order for
 89 hydraulic effects to be accurately captured (Pratt et al., 2008).

90 To take into account the role of upper layers, we consider a shallow-water model for multiple
 91 homogeneous layers with thicknesses h_j , densities ρ_j , and velocities $\vec{u}_j \equiv (u_j, v_j)$, where $j = 1, 2, 3$
 92 indicates the different layers; z is the vertical coordinate (positive upward); t is the time; $b(x,y)$ is the
 93 sea bottom, with $\frac{\partial b}{\partial x} \ll \frac{\partial b}{\partial y}$ and $W_j(x)$ being the cross-channel layer widths (Fig. 2a).

94 The hydrostatic pressure related to the third layer ($j = 3$) can be written as (Hogg, 1983; A01)

95

$$96 \quad p_3 = p_0'' + g \rho_3 (h_3 - z) + g \rho_2 (h_2 - h_3) + g \rho_1 (h_1 - h_2) \quad (1)$$

97

98 where p_0'' is a constant and g is the gravitational acceleration (m s^{-2}) (Fig. 2a).

99 The full shallow-water equation for a streamline in the third layer is as follows (Gill, 1982, p.
 100 231–232; Pratt et al., 2008):

101

$$102 \quad \delta \frac{\partial}{\partial t} u_3 + \delta u_3 \frac{\partial}{\partial x} u_3 + \delta v_j \frac{\partial}{\partial y} u_3 - f v_3 = -\frac{1}{\rho_3} \frac{\partial}{\partial x} p_3 + \delta^* \frac{\vec{F}_3}{\rho_3} \quad (2a)$$

$$103 \quad \delta \frac{\partial}{\partial t} v_3 + u_3 \frac{\partial}{\partial x} v_3 + v_3 \frac{\partial}{\partial y} v_3 + f u_3 = -\frac{1}{\rho_3} \frac{\partial}{\partial y} p_3 + \delta^* \frac{\vec{F}_3}{\rho_3} \quad (2b)$$

$$104 \quad \delta \frac{\partial}{\partial t} h_3 + h_3 \frac{\partial}{\partial x} u_3 + h_3 \frac{\partial}{\partial y} v_3 = \delta^* E |u_3 - u_2|, \quad (2c)$$

105

106 where f is the Coriolis parameter; \vec{F}_3 and $E|u_3 - u_2|$ represent, respectively, friction and entrainment
 107 between adjacent layers; and E is a suitable entrainment parameter. In Eq. (2) $\delta = 0$ gives the steady,
 108 quasi-geostrophic approximation, while $\delta^* = 0$ leads to the inviscid case. \vec{F}_3 contains both inter-layer
 109 friction and bottom stress, schematizing the upper and lower friction, which mainly occurs at the
 110 boundaries of the bottom layer. These stresses induce both upper and lower Ekman spirals, in
 111 addition to some entrainment effects (Johnson and Ohlsen, 1994). We point out that entrainment
 112 should be also included in the momentum budget (2a and 2b). Since friction with the overlying layer is
 113 included, the momentum impact of entrainment (entrainment drag) has indeed a potential role.
 114 However, this results in being another term that is lumped into a residual and we therefore omit such a
 115 term.

116 A general formulation for bottom friction can be defined as (Baringer and Price, 1997a, b; A01)

117

$$118 \quad \vec{F}_3 = -\rho_3 X(\vec{u}_3, h_3) \vec{u}_3, \quad (3)$$

119

120 where X (s^{-1}) is, in general, an empirical, nonlinear relation. In the following we will use the formulation

$$121 \quad X = K^* \frac{\rho \bar{u}}{h} - \text{with } K^* = \text{constant} - \text{that takes account for the averaged flow thickness and velocity}$$

122 (A01).

123

124 Ekman transport effects induced by the intermediate layer to the bottom layer, and how strong
 125 this transport is with respect to the geostrophic flow (i.e., thermal wind), can be explored by means of
 126 Ekman layer thickness $h_{EK} \approx (2\nu/f)^{1/2}$. For a laminar case (Johnson et al., 1976) such a thickness is \approx
 127 $O(10^{-1})$ m, where ν is the fluid viscosity. All this enlightens that for our case study the Ekman transport
 128 effect induced by the LIW to the EMDW is negligible. On the other hand we stress that the effect of
 129 friction in the bottom layer is more complex, mostly in the sill region. Real seafloors are indeed
 130 irregular, with bathymetric heterogeneities of many space scales. This gives a much thicker benthic
 131 layer, i.e., $(2K/f)^{1/2} \approx O(10)$ m for a turbulent viscosity $K \gg \nu$ (Salon et al., 2008). Moreover, Johnson
 et al. (1976) noted the occurrence of a secondary, frictional-induced cross-channel circulation, which

132 forces spun-down fluid into the interior, further limiting the sill flow (see Fig. 5 of Johnson and Ohlsen,
133 1994).

134 Vorticity is therefore strongly affected by these frictional effects. Moreover, because the bottom
135 frictional coefficient K^* may reasonably vary along-stream due to the spatial pattern of bottom
136 irregularities, the effect of friction on flow vorticity and PV further increases.

137

138 **3 The vorticity equation**

139 By focusing on the narrow bottom layer ($j = 3$, where the index “3” will be disregarded hereafter), we
140 make use of a stream-tube model (Fig. 2b) in a stream-wise coordinate system (ξ, ψ) . In this frame, ξ
141 is the along-flow coordinate, centered along the midline of the vein, and ψ is the cross-flow coordinate
142 (Smith, 1975; Killworth, 1977). Such a model is that of a steady flow where the bottom water is
143 assumed to be well mixed. The flow has strong axial velocity nearly uniform over a cross-section of
144 the stream (i.e., $v \ll u$ is anti-symmetric and vanishes at the vein lateral boundaries $\psi = \pm W/2$;
145 Baringer and Price, 1997b). Consequently, the cross-stream scale is assumed to be much smaller
146 than the local radius of curvature of the stream axis. All this implies that the velocity of a stream line is
147 a function of ξ only. The angle between the stream-tube axes (ξ, ψ) and the fixed axes (x, y) is β (Fig.
148 2b). Consequently, in this new frame, the horizontal gradient operator can be written as (Smith, 1975)

149

$$150 \quad \nabla_h = \left(\frac{1}{1-\psi} \frac{\partial}{\partial \xi}, \frac{\partial}{\partial \psi} - \frac{\frac{\partial \beta}{\partial \xi}}{1-\psi} \frac{\partial}{\partial \xi} \right) \approx \left(\frac{\partial}{\partial \xi}, \frac{\partial}{\partial \psi} \right) \quad (4)$$

151

152 where the approximation on the right-hand side of Eq. (4) is justified by a small $\psi \frac{\partial \beta}{\partial \xi}$, as for the Sicily

153 Channel case (Fig. 1), where β is close to zero because of the straight E–W path of the bottom vein
154 (see Sect. 7).

155 By cross-differentiating the horizontal components of Eq. (2), for a dense water streamline one
156 obtains the classical vorticity equation (Gill, 1982; p. 231)

157

$$158 \quad \frac{d}{dt} \zeta + (\zeta + f)(\text{div } \bar{u}) = \frac{1}{\rho} (\text{curl } \bar{F})_z, \quad (5)$$

159

160 which, in steady state, is

161

162
$$u \frac{\partial}{\partial \xi} \zeta + (\zeta + f)(\text{div } \bar{u}) = \frac{1}{\rho} (\text{curl } \bar{F})_z \quad (6)$$

163

164 It is useful to recall that ζ , in Eqs. (5) and (6), is the sum of a “shear vorticity”, related to the lateral
 165 shear of the current, and a “curvature vorticity” due to the bending streamline of the current (Holton,
 166 1972; Chen et al., 1992). The frictional term in Eqs. (5) and (6) can be explicated as

167
$$\frac{1}{\rho} (\text{curl } \bar{F})_z = -X\zeta .$$
 We finally emphasize that our Eq. (6) looks rather different from the steady,

168 quasi-geostrophic, and inviscid version proposed by Hogg (1983):

169

170
$$\left(\frac{\partial v}{\partial \xi} + f \right) u - \frac{\partial}{\partial \psi} B = 0 \quad (7)$$

171

172 where $B = \frac{p}{\rho} + \frac{v^2}{2}$ is the Bernoulli function.

173 Equation (6), once integrated, gives an exact diagnostic relation for the spatial evolution of ζ by
 174 assuming the knowledge of $h(\xi, \psi)$ and $u(\xi, \psi)$:

175

176
$$\frac{\zeta}{f} = e^{-\int_0^{\xi} \frac{1}{u} (X + \text{div } \bar{u}) dx} \left\{ \frac{\zeta_0}{f} - \int_0^{\xi} e^{\int_0^{x'} \frac{1}{u} (X + \text{div } \bar{u}) dx'} \frac{1}{u} (\text{div } \bar{u}) dx \right\} \quad (8)$$

177

178

179 Let us also note that an approximated solution of Eq. (6) for $\zeta \ll f$ is

180

181
$$\frac{\zeta}{f} = e^{-\int_0^{\xi} \frac{X}{u} dx} \left\{ \frac{\zeta_0}{f} - \int_0^{\xi} e^{\int_0^{x'} \frac{X}{u} dx'} \frac{1}{u} (\text{div } \bar{u}) dx \right\} \quad (9)$$

182

183 Intuitively, the two solutions Eqs. (8) and (9) are rather similar, although Eq. (9), analytically speaking,
 184 is relatively more subject to eventual irregularities in the flow velocity u , such as sharp and large peaks
 185 around the sill region. Moreover, we note that the approximation that leads to Eq. (9) cannot be
 186 applied near the sill of a channel if the flow there is subject to hydraulic control.

187 In real field cases, the knowledge of $h(\xi, \psi)$ and $u(\xi, \psi)$ is often difficult to infer from in situ
 188 hydrographic data. By seeking for a more applicable relation we therefore consider cross-sectional
 189 averages of the various terms of Eq. (6). This leads to the following solution for $\bar{\zeta} \ll f$ (Appendix A):
 190

$$191 \quad \frac{\bar{\zeta}}{f} = e^{-\int_0^{\xi} \frac{X}{\bar{u}} dx} \left\{ \frac{\bar{\zeta}_0}{f} - \int_0^{\xi} e^{\int_0^x \frac{X}{\bar{u}} dx'} \frac{1}{\bar{u}} (\overline{div \bar{u}}) dx \right\} \quad (10)$$

192
 193 where the overbars indicate the cross-channel average.

194 Such a cross-averaging approach is further justified by the fact that the bottom vein is
 195 assumed to flow along a narrow and long channel, where the longitudinal length scale is greater than
 196 the transversal one. In this way, one can diagnose the cross-channel average of flow vorticity ($\bar{\zeta}$)
 197 from the experimental knowledge of the cross-channel averaged \bar{h} and \bar{u} , which are bulk quantities
 198 easily inferable from in situ measurements. Moreover, the cross-channel averaging allows for further
 199 perturbations to be avoided that can be given by waves occurring along the lateral edges of the
 200 current, which are known, however, to have a small local effect (Lacombe and Richez, 1982; Pratt et
 201 al., 2008). Similar discussions can be had regarding the presence of upper and bottom Ekman
 202 boundary layers, which can perturb the non-averaged vorticity field, as was found in the study of
 203 Johnson and Ohlsen (1994).

204 205 **4 Continuity equation and vertical entrainment**

206 To include dynamical effects due to entrainment between the two lowest, cross-sectionally
 207 homogeneous layers, we consider here the mass continuity equation (Appendix A)

$$208 \quad \frac{d}{dt} \bar{h} + \overline{h \, div \bar{u}} = E |\bar{u} - \bar{u}_2| \quad (11)$$

209
 210
 211 or, in steady state,

$$212 \quad \bar{u} \frac{\partial}{\partial \xi} \bar{h} + \overline{h \, div \bar{u}} = E |\bar{u} - \bar{u}_2| \quad (12)$$

213
 214
 215

216 where $E|\bar{u} - \bar{u}_2|$ describes the vertical displacement of the interface between the two lowest layers
 217 due to mixing. Layer 2 (i.e., the middle layer; Fig. 2a) has velocity $(\bar{u}_2, 0)$, and the entrainment
 218 dimensionless parameter E is assumed to be $\sim 10^{-4}$ (Ellison and Turner, 1959; Turner, 1986).
 219 Entrainment also implies an exchange of momentum between layers, and thus an additional resistive
 220 force (Baringer and Price, 1997b; Gerdes et al., 2002) that should be considered in the momentum
 221 balance. However, if \bar{u} is $\sim \bar{u}_2$ (Tables 1 and 2), momentum variations due to entrainment can be
 222 reasonably neglected as previously discussed.

223 We finally point that the continuity Equations (11) and (12) can be formulated if one assumed
 224 that both velocity and density profiles within the bottom layer exhibit similarity forms, so that the rate of
 225 entrainment may be related solely to the mean velocity and the layer thickness (Smith, 1975).

226

227 5 Vorticity equation with entrainment

228 By substituting the $\overline{\text{div}\bar{u}}$ in Eq. (10) with that from Eq. (12), one obtains

229

$$230 \frac{\bar{\zeta}}{f} = \frac{\bar{u}_0}{\bar{u}} e^{-\int_0^{\bar{\zeta}} \frac{X}{\bar{u}} dx} \left(\frac{\bar{\zeta}_0}{f} + \frac{1}{\bar{u}_0} \int_0^{\bar{\zeta}} e^{\int_0^{X'} \frac{X}{\bar{u}} dx'} \left[\frac{\bar{u}}{h} \frac{d\bar{h}}{dx} - \frac{1}{h} E(\bar{u} - \bar{u}_2) \right] dx \right), \quad (13a)$$

231

232 while, disregarding the entrainment, equations (10) and (12) simply give

233

$$234 \frac{\bar{\zeta}}{f} = \frac{\bar{u}_0}{\bar{u}} e^{-\int_0^{\bar{\zeta}} \frac{X}{\bar{u}} dx} \left(\frac{\bar{\zeta}_0}{f} + \frac{1}{\bar{u}_0} \int_0^{\bar{\zeta}} e^{\int_0^{X'} \frac{X}{\bar{u}} dx'} \frac{\bar{u}}{h} \frac{d\bar{h}}{dx} dx \right) \quad (13b)$$

235

236 Note that, for the sake of simplicity, we hereafter omit overbars on all the cross-channel averaged
 237 variables.

238 Equations (13a) and (13b) show that the main forcing on ζ is given by (i) a vorticity stretching

239 term $\frac{u}{h} \frac{\partial h}{\partial \xi}$ (Gill, 1977), (ii) the entrainment effect, and (iii) friction. In particular, we note that:

240 1. ζ is the sum of an initial condition (ζ_0) plus the integral of both stretching and entrainment

241 terms $\left[\frac{u}{h} \frac{dh}{dx} - \frac{1}{h} E(u - u_2) \right]$ due to bathymetric forcing and vertical mixing, respectively;

242 2. the entrainment term $\frac{1}{h}E(u-u_2)$ is, however, small for $u \approx u_2$, a condition that occurs when
 243 the two adjacent bottom and intermediate layers flow in the same direction;

244 3. both initial condition and stretching terms are multiplied by $\frac{u}{u_0} e^{-\int_0^\xi \frac{X}{u} dx}$, which is related to
 245 friction, and it vanishes progressively over a distance $\sim 3u/X$. One can therefore argue that the role of
 246 frictional effects largely depend on the friction function X and thus on the local sea-bottom roughness.
 247 All these features are particularly valid where topographic changes are significant and therefore
 248 represent general effects for deep, steady, baroclinic currents in marine channels, straits, and ridges.

249 Our considerations imply that the evolution of ζ/f is not strictly related to the initial or
 250 downstream conditions but rather that it is mainly ruled by $\frac{u}{h} \frac{\partial h}{\partial x}$. Indeed, upstream of the sill of a

251 marine channel $\frac{u}{h} \frac{\partial h}{\partial \xi} \leq 0$, while $\frac{u}{h} \frac{\partial h}{\partial \xi}$ becomes positive downstream, which means that ζ must
 252 decrease as the sill is approached, eventually becoming negative. Once downstream of the sill, ζ will
 253 increase again, reaching pre-existing upstream values. This is an important point since it differs from
 254 classical stream-tube models that require, for hydraulically supercritical flows, the integral from the
 255 upstream location to be taken in order to obtain solutions for ζ . Moreover, "if the ordinary differential
 256 equation can be solved analytically in closed form, the constant of integration in the analytic solution
 257 can be determined from the boundary condition; consequently the location of the control section,
 258 where the boundary condition is prescribed, is of no concern" (Jain, 2001).

259

260 6 PV equation

261 By combining Eqs. (5) and (11), for cross-section averaged quantities, one obtains the shallow-water
 262 vertical PV equation

263

$$264 \left(\frac{d}{dt} + \Gamma \right) \Pi = \frac{(\text{curl} \vec{F})_z}{\rho h} = -\frac{X \zeta}{h}, \text{ with } \Pi = \frac{\zeta + f}{h} \text{ and } \Gamma = \frac{E|u - u_2|}{h}. \quad (14)$$

265

266 In a steady case, Eq. (15) gives

267

$$268 \Pi = e^{-\int_0^\xi \frac{\Gamma}{u} dx} \left\{ \Pi_0 - \int_0^\xi e^{\int_0^{x'} \frac{\Gamma}{u} dx'} \frac{X \zeta}{hu} dx' \right\}, \quad (15a)$$

269

270 which can be significantly simplified if the exponential length scale u/Γ in Eq. (15a) is much larger
271 than the channel length:

272

$$273 \quad \Pi \approx \Pi_0 - \int_0^{\xi} \frac{X\zeta}{hu} dx. \quad (15b)$$

274

275 Equations (16a) and (16b) confirm that variations in ζ and h , along with frictional effects
276 represented by the presence of X , play a direct role in Π variations. Moreover, because u , h , and X
277 are, in general, rather regular and positive quantities, while ζ is much more variable, Eqs. (14) and
278 (15) suggest that for positive ζ and weak friction – as occurs upstream of a sill – Π must decrease; for
279 a negative ζ and strong friction at the sill region, Π increases.

280

281 **7 Diagnostic analysis in the Sicily Channel**

282 We now analyze Eqs. (14) and (16), namely $\zeta(\xi)$ and $\Pi(\xi)$, for the realistic case of the EMDW flowing
283 through the Sicily Channel (Fig. 1).

284

285 **7.1 Sicily Channel hydrographic settings**

286 Cross-channel vertical sections of potential temperature (θ) and salinity (S) along the whole Sicily
287 Channel were performed by A01 during MATER II (10–31 January 1997) and MATER IV (21 April–14
288 May 1998) cruises (Fig. 1a) in order to investigate the three-layer flow properties, in particular, around
289 the [west](#) sill (Figs. 3 and 4). CTD casts were collected over a regular grid (CTD stations ~ 9 km apart
290 from each other; near the sill the distance was reduced to ~ 5 km).

291 The analysis of potential density (σ), θ , and S , combined with the assumption that the LIW flux
292 is conserved, allowed A01 to estimate the [thickness and cross-sectional areas of EMDW, LIW, and](#)
293 [MAW layers](#) (Table 1). [Current meter measurements were also collected over the western sill \(i.e.,](#)
294 [section IV\) and in correspondence with section V \(Figs. 1, 3, and 4\). These measurements allowed to](#)
295 [estimate EMDW and LIW velocities for all sections by the use of continuity. The upper part of LIW was](#)
296 [defined by \$\sigma \sim 28.80\$ and the interface between LIW and EMDW by \$\sigma \sim 29.11\$ – \$29.16\$ \(Figs. 3 and 4\).](#)
297 [The EMDW was defined by using \$\theta\$ - \$S\$ diagrams, recognizing the bottom density observed along each](#)
298 [transect.](#)

299 A01 analysis showed that the EMDW enters the channel from the east at a depth of ~ 400 – 550
300 m, [banked against the Sicilian shelf break](#) (Figs. 1b, 3, and 4). There, the width (W) of the current is
301 about 20 km, σ is ~ 29.17 , the cross-channel averaged velocity \bar{u} is $12 - 13 \text{ cm s}^{-1}$, and the cross-

302 channel averaged thickness \bar{h} is $\sim 75 - 120\text{m}$ (Tables 1 and 2). Further west, the EMDW was
303 observed to sink to depths greater than 700m (transect III in Figs. 3 and 4), rising again at 300–350m
304 depth at the western sill but, rather surprisingly, **banked against the Tunisian shelf break** (transects
305 IV–V). There, W is $\sim 8\text{--}15\text{ km}$, σ is ~ 29.15 , \bar{h} is $\sim 25\text{--}50\text{ m}$, and \bar{u} reaches $\sim 27\text{--}46\text{ cm s}^{-1}$. At the
306 western mouth of the channel the EMDW sinks again along the Sicilian coast at $\sim 1100\text{--}1200\text{m}$
307 (transect VII). Then, it attains a buoyancy equilibrium in the southern Tyrrhenian Sea, where W is ~ 20
308 km, σ is ~ 29.12 , \bar{u} is $\sim 8\text{--}17\text{ cms}^{-1}$, and \bar{h} is $\sim 130\text{--}200\text{m}$ (Sparnocchia et al., 1999; Figs. 3 and 4).
309 This final sinking is allowed by the small density of the Tyrrhenian LIW ($\sigma \sim 29.05$).

310 The initial θ – S characteristics of the EMDW at the eastern entrance are progressively modified
311 along the vein route (Figs. 3 and 4). These changes are rather weak east of the sill and within the
312 channel, while they become larger in the region west of the sill. **The most substantial changes in the**
313 **hydrographic characteristics are observed between sections V and VII: a gradual increase of both**
314 **temperature and salinity, indicates a progressive lightening of EMDW from section I (eastern sill) to**
315 **section IV. This stresses the important role of friction and mixing around the sill region in modifying the**
316 **hydrographic characteristics of the bottom water and, in turn, enlightens a rather weak mixing**
317 **processes that is fully discussed in A01.**

318 From these data, A01 also estimated Rossby ($Ro \sim 0.1$) and Froude numbers. Far from the sill
319 the EMDW was characterized by a Froude number of $Fr \sim 0.1$, a small value that would inhibit a strong
320 mixing between LIW and EMDW. Over the sill Fr is $\sim 0.6\text{--}0.8$ (Tables 1 and 2). These values,
321 however, are obtained from time averaging and thus depict a steady condition (A01). We believe that
322 Fr may reach higher values during strong transient phenomena.

323 Finally, by assuming quadratic friction, $\vec{F} = -K^* \frac{\rho \bar{u}}{\bar{h}} \vec{u}$, A01 estimated a dimensionless
324 frictional coefficient, $K^* = 2.6 \times 10^{-2}$, from the vein momentum balance. This value is rather large with
325 respect to those proposed in the literature – which lie within the range of $2\text{--}12 (\times 10^{-3})$ (Baringer and
326 Price, 1997b) – and is likely justified by the very irregular topography of the Sicily Channel around the
327 sill region.

328

329 **7.2 Diagnostic analysis for vorticity and PV**

330 From hydrographic and current-meter data for the EMDW above described we perform a scale
331 analysis of Eq. (5): considering $L \sim 10^5\text{ m}$ and $W \sim 10^4\text{ m}$ as the along-channel and cross-channel
332 space scale, respectively, and $U \sim 10^{-1}\text{ ms}^{-1}$ as the along-channel velocity, we obtain

333

$$\begin{aligned}
& u \frac{\partial}{\partial x} \zeta + (\zeta + f) (\text{div} \bar{u}) = -X\zeta \\
334 \quad & \frac{U}{L} \left(\frac{U}{R} + \frac{U}{W} \right) + \left(\frac{U}{R} + \frac{U}{W} + f \right) \left(\frac{U}{L} \right) = X \left(\frac{U}{R} + \frac{U}{W} \right) \quad (16) \\
& \frac{1}{T} (10^{-6} + 10^{-5}) + \frac{1}{T} (10^{-6} + 10^{-5} + 10^{-4}) = 10^{-5} \times 10^{-4}
\end{aligned}$$

335

336 where $T \sim 10^{4-5}$ s is the EMDW timescale, f is $\sim 10^{-4} \text{ s}^{-1}$, and $R \sim 10^5$ m is an estimated curvature
337 radius for the EMDW pathway around the sill region; the friction coefficient $X \sim 10^{-5} \text{ s}^{-1}$ is estimated by
338 considering the value proposed by A01 (i.e., K^*), multiplied by $U^2/H \sim 10^{-4} \text{ s}^{-1}$ (where $H \sim 100$ m scales
339 for the EMDW thickness). We remark that ζ in Eq. (16) is the sum of a “shear vorticity” ($U/W \sim 10^{-5} \text{ s}^{-1}$
340 in the Sicily Channel) and a “curvature vorticity” ($U/R \sim 10^{-6} \text{ s}^{-1}$ in the Sicily Channel) due to the
341 bending pathway of the EMDW.

342 The scale analysis in Eq. (16) shows that each term of Eq. (5), and thus of Eq. (14), plays a
343 role in the EMDW dynamics. Friction, in particular, results in being a crucial term in the along-channel
344 evolution of ζ and it brings to a non-conservative PV. Moreover, since (i) $\zeta \ll f$ in Eq. (16), (ii) $u \approx u_2$ in
345 Eq. (13a), and (iii) the length scale $u\Gamma \sim 10^6$ m in Eq. (15) results in being larger than the entire
346 channel length, one can reasonably use the approximated solutions for vorticity and PV in Eqs. (13b)
347 and (15b). From these considerations we therefore expect a negative trend for ζ when approaching
348 the sill region, followed by a positive trend and a rather large peak of Π immediately after the sill, as
349 confirmed by the detailed results we describe below. The following analysis of Eqs. (13) and (15) in
350 their closed form is performed by using continuous functions for $u(\xi)$ and $h(\xi)$, which are computed
351 from modified spline interpolations of \bar{u}_i and \bar{h}_i as obtained from the in situ data (Appendix B).
352 Velocity interpolations are also compared with PROTHEUS numerical data (Fig. 5), a relatively coarse
353 resolution Mediterranean model ($1/8^\circ \times 1/8^\circ$) based on the MIT general circulation model (MITgcm;
354 Sannino et al., 2009; Sannino, personal communication), and show fair agreement with the splines.
355 Due to the coarse vertical resolution of this model, such a comparison cannot be provided for the
356 bottom water thickness \bar{h}_i .

357

358 **MATER II cruise (January 1997)**

359 For this data set (Figs. 3 and 5, Table 3) we see that both ζ and Π are rather small upstream of the sill,
360 namely $\zeta \sim 5 \times 10^{-6} \text{ s}^{-1}$ or less and $\Pi \sim 8 \times 10^{-7} \text{ s}^{-1} \text{ m}^{-1}$ (Fig. 6). Approaching the sill, vorticity changes
361 sign (Fig. 6) due to the stretching term $\frac{u}{h} \frac{\partial h}{\partial \xi}$ in Eq. (13). A negative value $\zeta \sim -6 \times 10^{-5} \text{ s}^{-1}$ is then
362 reached at transect IV, and consequently Π reaches a very large peak $\sim 6 \times 10^{-6} \text{ s}^{-1} \text{ m}^{-1}$ at transect V.

363 Downstream of the sill, in the southern Tyrrhenian Sea, ζ again has a positive value, $\zeta \sim 6 \times 10^{-5} \text{ s}^{-1}$,
364 and Π strongly decreases to $8 \times 10^{-7} \text{ s}^{-1} \text{ m}^{-1}$ (Fig. 6).

365

366 **MATER IV cruise (April–May 1998)**

367 This springtime data set (Figs. 4 and 5, Table 4), although similar to the one described above, shows
368 lower velocities and fluxes than those of the winter case (Fig. 6; Stansfield et al., 2001). Upstream of
369 the sill ζ is $\sim 5 \times 10^{-6} \text{ s}^{-1}$ and Π is $\sim 1 \times 10^{-6} \text{ s}^{-1} \text{ m}^{-1}$, while, for a region about 120 km long before the sill,
370 ζ goes from $\sim 10^{-6}$ to $-7 \times 10^{-5} \text{ s}^{-1}$. In the same way, Π goes from $\sim 10^{-6} \text{ s}^{-1} \text{ m}^{-1}$ to $\sim 6 \times 10^{-6} \text{ s}^{-1} \text{ m}^{-1}$
371 immediately after the sill (Fig. 6). In the southern Tyrrhenian Sea, downstream of the sill, $\zeta \sim 4 \times 10^{-5}$
372 s^{-1} . This shows a sudden change in vorticity, as for the MATER II cruise data (Fig. 6). Accordingly, Π
373 decreases strongly from the largest value at the sill to $\sim 1.5 \times 10^{-6} \text{ s}^{-1} \text{ m}^{-1}$ in the Tyrrhenian Sea, and
374 then strongly decreases.

375

376 **8 Discussions**

377 The lack of specific current-meter measurements does not allow for a realistic determination of
378 vorticity and, in particular, for a validation of our model. [Moreover, the use of available numerical](#)
379 [outputs in order to validate and/or compare our analytic results is not an easy task due to grid](#)
380 [problems \(Dr. G. Sannino, personal communication, 2015; Dr. L. Palatella, personal communication,](#)
381 [2015\): spatial \(vertical and horizontal\) resolutions are often too coarse and, in particular, bottom](#)
382 [velocities are available on a very few cross-stream grid points \(i.e., one or two at the western sill\).](#)

383 A rough, although reasonable, way to infer the EMDW vorticity independently from our model
384 is given by the following considerations: since the EMDW path is rather straight upstream of the sill
385 (Fig. 1), the curvature vorticity of this flow along the upstream region of the channel is very small
386 (Holton, 1972). Therefore, initial values of vorticity for our analysis are taken from the shear vorticity
387 only, which is approximately $\zeta_0 \sim U/W$ (Fig. 6). Although this approximation – taken as an initial
388 condition for our vorticity analysis – can be affected by a large error, Eq. (13) shows that the “memory”
389 of the initial vorticity ζ_0 vanishes within a few kilometers.

390 A different option for determining ζ is suggested through use of the classical Π conservation:

391 $\zeta = \frac{f h}{h_\infty} - f$ (Gill, 1982), where h_∞ is the bottom depth far upstream, in the Ionian Sea. This suggests

392 that a vorticity stream-wise profile should look approximately like the EMDW thickness profile.
393 However, such an estimate of ζ only holds far from the sill, where friction and mixing certainly do not
394 affect the deep current.

395 [Our diagnosis, through use of the A01 experimental data set, confirms the “memory-loss”](#)
396 [effect of upstream vorticity conditions due to the role of friction.](#) We found that the region around the

397 sill (~ 70 km length) has an unexpected negative peak of ζ that, moreover, seems to be also in
 398 agreement with the EMDW–LIW interface tilting that occurs at the sill (Figs. 3 and 4) in terms of
 399 change in flow curvature.

400 Abrupt changes in vorticity are also reflected in the downstream evolution of PV, which is
 401 definitely not constant around the sill region. This interesting result points out that an increase in Π
 402 violates the all those assumptions for flow stability theorems (see, for instance, Wood and McIntyre,
 403 2010).

404 An interesting aside, we check the reliability of the idealized friction coefficient by investigating the
 405 balance of the PV Eq. (14) for the EMDW along-channel evolution. The nonlinear friction

406 $\vec{F} = -K^* \frac{\rho \bar{u}}{h} \bar{u}$ described above, with the constant friction coefficient $K^* = 2.6 \times 10^{-2}$ (A01), gives the

407 following PV balance:

408

$$409 \left(\frac{d}{dt} + \Gamma \right) \Pi = \frac{(\text{curl} \vec{F})_z}{\rho h} \approx -\frac{2K^* u \zeta}{h^2} \sim 10^{-11} \text{ m}^{-1} \text{ s}^{-2}. \quad (17)$$

410

411 Equation (17) is nicely satisfied in the upstream part of the Sicily Channel, while this agreement fails
 412 over the sill (Fig. 7). Therefore, to investigate such a discrepancy, we analyze

413

$$414 \begin{aligned} \varepsilon &= \left(u \frac{\partial}{\partial \xi} + \Gamma \right) \frac{\zeta + f}{h} - \frac{(\text{curl} \vec{F})_z}{\rho h} = \left(u \frac{\partial}{\partial \xi} + \Gamma \right) \frac{\zeta + f}{h} + \frac{2K^*}{h^2} u \zeta \\ &= \underbrace{u \frac{d}{d\xi} \Pi}_{\varepsilon_1} + \underbrace{\Gamma \Pi}_{\varepsilon_2} + \underbrace{\frac{2K^*}{h^2} u \zeta}_{\varepsilon_3} \approx 10^{-10} - 10^{-11} \text{ s}^{-2} \text{ m}^{-1} \end{aligned} \quad (18)$$

415

416 We point out that the analysis of each term of Eq. (18) does not use the explicit solution for Π in Eqs.

417 (15a) and (15b) but only the vorticity $\zeta(\xi)$ in Eq. (13b) since $\Pi = \frac{\zeta + f}{h}$. All this represents therefore a

418 sort of independent validation of the PV balance (17).

419 For both MATER cruises, the along-channel profiles of the three terms ε_1 , ε_2 , and ε_3 (Fig. 7) are
 420 rather small but never exactly balanced, in particular around the sill region. For the MATER IV cruise,
 421 which was characterized by lower velocities, this unbalance seems to be due to the variability of the
 422 entrainment term ε_2 , when approaching the sill, and to the advection term ε_1 , which results in being too
 423 small for balancing the friction term ε_3 .

424 This suggests that some tuning of the quadratic friction coefficient is needed. Consequently,
425 we propose the use of a varying friction coefficient, namely $K^* \rightarrow K^* + X^*(\xi)$. Indeed, large values of ϵ
426 around the sill (Fig. 7) suggest that both local roughness due to the sea-bottom morphology over the
427 sill and an additional frictional effect due to the strong mixing occurring at the sill could affect the local
428 schematization for friction. To optimize the balance of Eq. (18), we set

$$430 \quad 0 = u \frac{d}{dx} \Pi + \Gamma \Pi + \frac{K^* + X^*(\xi)}{h^2} u, \quad (19)$$

431
432 which leads to local solutions for $X^*(\xi)$ (Fig. 8).

433 In the region where the bottom of the channel is rather flat, i.e., until 350 km from the beginning
434 of the channel (around transect IIIa, Fig. 1), one obtains $X^*(\xi) \ll K^*$, in good agreement with the A01
435 coefficient. Then, approaching the sill, a $\sim 50\%$ greater friction coefficient is required to satisfy Eq. (19)
436 (Fig. 8). We note that a similar approach for seeking a more realistic frictional coefficient along
437 particular morphological settings (such as straits and channels) was also pursued by Baringer and
438 Price (1997a, b). Their results showed that (i) “large bottom friction coupled with the relatively small
439 thickness of outflows may lead to a turbulent bottom boundary layer that extends over much of the
440 total thickness of the outflow” and (ii) “the bottom stress appears to follow a quadratic drag law, though
441 the appropriate c_D [i.e., dimensionless friction coefficient] will vary considerably with the type of
442 average velocity available for the parameterization”. Both conclusions are in agreement with our
443 results.

444 445 **9 Conclusions**

446 We investigated vorticity (ζ) and PV (Π) evolution of the EMDW flowing along the Sicily Channel by
447 making use of a shallow-water, stream-tube approach. The model allowed us to explore bottom
448 current properties under the effect of sea-bottom changes, bottom friction, and vertical entrainment.
449 Our analysis reveals sharp negative vorticity peaks over the sill region, while ζ again becomes positive
450 downstream of the sill, as they were in the eastern basin. All this reflects on the PV behavior of the
451 bottom currents, which experience large variations in Π , and reveals how PV-constant models are not
452 suitable for exploring bottom currents dynamics along rotating channels. We argue that the along-
453 channel evolution of both vorticity and PV is due to bathymetric effects occurring approaching the sill,
454 which are also modulated by frictional effects that significantly change the structure of vorticity and PV
455 equations for describing such dynamics.

456 Knowledge of the downstream evolution of ζ allowed us (i) to infer the deep vein dynamics, in
457 particular, around the sill region, where frictional, entrainment, and stretching effects all play a crucial

458 role; (ii) to diagnose the PV balance; and thus (iii) to tune the parameterization for bottom friction. In
 459 this regard, our analysis is a general implication of the steady, deep, and baroclinic current theory in
 460 marine straits (Smith, 1975; Killworth, 1977; Hogg, 1983) and it can provide an analytic support to
 461 numerical and tank experiments aimed to the investigation of rotating hydraulic dynamics.

462

463 **Appendix A: The cross-sectional averages**

464 We evaluate here the cross-sectional averages of various terms of the vorticity Eq. (7). Let us first

465 assume that, for a narrow and long strait or channel, the derivative $\frac{\partial}{\partial \psi} a \gg \frac{\partial}{\partial \xi} a$ cross-strait, where

466 a is a general flow property. We then define the cross-channel average as $\bar{a} = \int a dz d\psi$.

467 For a nonlinear friction $\vec{F} = -\rho_3 X(\bar{u}_3, h_3) \bar{u}_3$, the cross-channel averaging would therefore give

468

$$469 \quad \overline{\frac{1}{\rho} (\text{curl} \vec{F})_z} = K \frac{\bar{u}}{\bar{h}} \frac{\partial \bar{u}}{\partial \psi} = -K \frac{\bar{u}}{\bar{h}} \bar{\zeta} \equiv -X \bar{\zeta} \quad (\text{A1})$$

470

471 since \bar{u} and \bar{h} by definition are functions of ξ only.

472 Accordingly, the second term on the left-hand side of the vorticity Eq. (6) can be averaged by

473 considering that $\int d\psi \partial_\psi v = 0$ since v is symmetric and vanishes at the vein lateral borders.

474 Therefore, one obtains

475

$$476 \quad \overline{\text{div} \vec{u}} \equiv \int dz d\psi (\partial_\xi u + \partial_\psi v) = \int dz d\psi \partial_\xi u = \overline{\partial_\xi u} \quad (\text{A2})$$

477

478 This, moreover, results that

479

$$480 \quad \overline{\zeta \frac{\partial u}{\partial \xi} + u \frac{\partial \zeta}{\partial \xi}} = \iint \frac{\partial}{\partial \xi} (u \zeta) dz d\psi \approx \frac{\partial}{\partial \xi} \iint (u \zeta) dz d\psi \approx \frac{\partial}{\partial \xi} \bar{u} \iint \zeta dz d\psi = \bar{u} \frac{\partial \bar{\zeta}}{\partial \xi} + \bar{\zeta} \frac{\partial \bar{u}}{\partial \xi}$$

481

$$(\text{A3})$$

482

483 since u is less variable than ζ . All of this leads to the cross-averaged vorticity equation in the steady
 484 case

485

486
$$\bar{u} \frac{\partial}{\partial \xi} \bar{\zeta} + (f + \bar{\zeta}) \overline{\text{div} \bar{u}} \approx \frac{1}{\rho} \overline{(\text{curl} \bar{F})_z} = -X \bar{\zeta} \quad (\text{A4})$$

487

488 and thus to the corresponding solution, Eq. (10), in the main text for $\bar{\zeta} \ll f$.

489 Similarly, the mass conservation equation

490

491
$$u \frac{\partial}{\partial \xi} h + h \text{div} \bar{u} \approx E|u - u_2| \quad (\text{A5})$$

492

493 becomes Eq. (11) in the main text.

494

495 **Appendix B: The spline interpolation of the u_i and h_i**

496 To use the cross-averaged EMDW data of A01 (Tables 1 and 2), we computed a continuous $u(\xi)$ and
 497 $h(\xi)$ spline interpolation of the u_i and h_i from transect $i = 1, 2, \dots$ (Fig. 6). This problem may be solved
 498 exactly by fitting a polynomial of degree $n-1$. Unfortunately, for such a “polynomial” solution, it is not
 499 easy to control for the influence of any particular observation. Moreover, it can behave very strangely
 500 at the boundaries.

501 Spline interpolation achieves a better result. In order to enhance the spline flexibility around the
 502 sill, following Durbin and Koopman (2001) we introduce a scale parameter σ that varies as $\sigma^2 =$
 503 $v^2 + \mu \Lambda(\xi)$ with $\mu \gg v^2$. For such a “modified” spline interpolation, one has

504

505
$$\Lambda(\xi) = \frac{35}{32} \left[1 - \left(\frac{2(\xi - \Delta \xi_m)}{\xi_m - \xi_{m-1}} \right)^2 \right]^3, \text{ where } \Delta \xi_m = (\xi_m - \xi_{m-1})/2, \quad (\text{B1})$$

506

507 for all points in an interval $\xi_{m-1} < \xi < \xi_{m+1}$ and zero elsewhere. We moreover impose that our transect V
 508 is a local minimum for $h(\xi)$ and a maximum of $u(\xi)$ as shown in Fig. 6. Note that, although these last
 509 plots might look rather discontinuous over the sill, in reality this apparent effect is due to the vigorous
 510 evolution of the current over the sill. We moreover compare such a modified spline interpolation of u_i
 511 with monthly averaged data of PROTHEUS (see text). Along-channel velocities for January 1997 and
 512 April 1998 cruises are shown in Fig. 5, superimposed on modified spline interpolations of both MATER
 513 II and MATER IV.

514

515

516

517 *Author contributions.* E. Salusti developed the analytic theory with contributions of F. Falcini,
518 who also performed the vorticity and PV diagnosis. Both authors prepared the manuscript.

519

520 *Acknowledgements.* We thank M. Astraldi and G. P. Gasparini for help and criticism, and V. Rupolo
521 and G. M. Sannino for the PROTHEUS data. Many thanks are also due to M. Kurgansky, L. Pratt and
522 R. Wood for suggestions about potential vorticity dynamics, as well as to T. Proietti for discussion
523 regarding the spline interpolations. This work has been funded supported by the RITMARE Italian
524 Research Ministry (MIUR) Projects.

525

526

527 **References**

528 Armi, L., & Farmer, D. (1985). The internal hydraulics of the Strait of Gibraltar and associated sills and
529 narrows. *Oceanologica Acta*, 8(1), 37-46.

530 Astraldi, M., Gasparini, G. P., Gervasio, L., & Salusti, E. (2001). Dense water dynamics along the
531 Strait of Sicily (Mediterranean Sea). *Journal of physical oceanography*, 31(12), 3457-3475.

532 Baringer, M. O. N., & Price, J. F. (1997). Mixing and spreading of the Mediterranean outflow. *Journal*
533 *of Physical Oceanography*, 27(8), 1654-1677.

534 Baringer, M. O. N., & Price, J. F. (1997). Momentum and energy balance of the Mediterranean
535 outflow. *Journal of Physical Oceanography*, 27(8), 1678-1692.

536 Borenäs, K., & Lundberg, P. (1986). Rotating hydraulics of flow in a parabolic channel. *Journal of Fluid*
537 *Mechanics*, 167, 309-326.

538 Borenäs, K. M., & Lundberg, P. A. (1988). On the deep-water flow through the Faroe Bank Channel.
539 *Journal of Geophysical Research: Oceans* (1978–2012), 93(C2), 1281-1292.

540 Bryden, H. L., & Kinder, T. H. (1991). Steady two-layer exchange through the Strait of Gibraltar. *Deep*
541 *Sea Research Part A. Oceanographic Research Papers*, 38, S445-S463.

542 Chen, C., Beardsley, R. C., & Limeburner, R. (1992). The structure of the Kuroshio southwest of
543 Kyushu: velocity, transport and potential vorticity fields. *Deep Sea Research Part A. Oceanographic*
544 *Research Papers*, 39(2), 245-268.

545 Durbin, J., & Koopman, S. J. (2012). *Time series analysis by state space methods* (No. 38). Oxford
546 University Press.

547 Ellison, T. H., & Turner, J. S. (1959). Turbulent entrainment in stratified flows. *Journal of Fluid*
548 *Mechanics*, 6(03), 423-448.

549 Gerdes, F., Garrett, C., & Farmer, D. (2002). On internal hydraulics with entrainment. *Journal of*
550 *physical oceanography*, 32(3), 1106-1111.

551 Gill, A. E. (1977). The hydraulics of rotating-channel flow. *Journal of Fluid Mechanics*, 80(04), 641-
552 671.

553 Gill, A. E. (1982). *Atmosphere-ocean dynamics* (Vol. 30). Academic press. pp. 662.

554 Hogg, N. G. (1983). Hydraulic Control and Flow Separation in a Multi-Layered Fluid with Applications
555 to the Vema Channel. *Journal of Physical Oceanography*, 13(4), 695-708.

556 Holton. J.R. (1972). *Introduction to dynamic meteorology* . Academic Press, pp 319 .

557 Jain, S.C. (2001). *Open-channel Flows*. John Wiley & Sons pp. 328.

558 Johnson, G. C., & Ohlsen, D. R. (1994). Frictionally modified rotating hydraulic channel exchange and
559 ocean outflows. *Journal of Physical Oceanography*, 24(1), 66-78.

560 Johnson, D. A., McDowell, S. E., Sullivan, L. G., & Biscaye, P. E. (1976). Abyssal hydrography,
561 nephelometry, currents, and benthic boundary layer structure in the Vema Channel. *Journal of*
562 *Geophysical Research*, 81(33), 5771-5786.

563 Killworth, P. D. (1977). Mixing of the Weddell Sea continental slope. *Deep Sea Research*, 24(5), 427-
564 448.

565 Killworth, P. D. (1992). Flow properties in rotating, stratified hydraulics. *Journal of physical*
566 *oceanography*, 22(9), 997-1017.

567 Lacombe, H., & Richez, C. (1982). The regime of the Strait of Gibraltar. *Elsevier Oceanography*
568 *Series*, 34, 13-73.

569 Paldor, N. (1983). Stability and stable modes of coastal fronts. *Geophysical & Astrophysical Fluid*
570 *Dynamics*, 27(3-4), 217-228.

571 Pratt, L. J., Helfrich, K. R., & Leen, D. (2008). On the stability of ocean overflows. *Journal of Fluid*
572 *Mechanics*, 602, 241-266.

573 Pratt, L. L., & Whitehead, J. A. (2007). *Rotating hydraulics: nonlinear topographic effects in the ocean*
574 *and atmosphere* (Vol. 36). Springer.

575 Salon, S., Crise, A., & Van Loon, A. J. (2008). Dynamics of the bottom boundary layer. *Contourites.*
576 *Developments in Sedimentology*, 60, 83-98.

577 Sannino, G., Herrmann, M., Carillo, A., Rupolo, V., Ruggiero, V., Artale, V., & Heimbach, P. (2009). An
578 eddy-permitting model of the Mediterranean Sea with a two-way grid refinement at the Strait of
579 Gibraltar. *Ocean Modelling*, 30(1), 56-72.

580 Smith, P. C. (1975). A streamtube model for bottom boundary currents in the ocean. In *Deep Sea*
581 *Research and Oceanographic Abstracts* (Vol. 22, No. 12, pp. 853-873). Elsevier.

582 Sparnocchia, S., Gasparini, G. P., Astraldi, M., Borghini, M., & Pistek, P. (1999). Dynamics and mixing
583 of the Eastern Mediterranean outflow in the Tyrrhenian basin. *Journal of Marine Systems*, 20(1), 301-
584 317.

585 Stansfield, K., Smeed, D. A., Gasparini, G. P., McPhail, S., Millard, N., Stevenson, P., ... & Rabe, B.
586 (2001). Deep-sea, high-resolution, hydrography and current measurements using an autonomous
587 underwater vehicle: The overflow from the Strait of Sicily. *Geophysical Research Letters*, 28(13),
588 2645-2648.

589 Turner, J. S. (1986). Turbulent entrainment: the development of the entrainment assumption, and its
590 application to geophysical flows. *Journal of Fluid Mechanics*, 173, 431-471.

591 Whitehead, J. A., Leetmaa, A., & Knox, R. A. (1974). Rotating hydraulics of strait and sill flows†.
592 *Geophysical and Astrophysical Fluid Dynamics*, 6(2), 101-125.

593 Whitehead, J. A. (1998). Topographic control of oceanic flows in deep passages and straits. *Reviews*
594 *of Geophysics*, 36(3), 423-440.

595 Wood, R. & McIntyre, M. (2010). A general theorem on angular momentum changes due to potential
596 vorticity mixing and on potential energy changes due to buoyancy mixing. *Journal Atm. Scienc.*, 67,
597 1261-1274.

598
599
600
601
602
603
604
605
606
607
608

Transect	I	II	III	IV	V	VIc	VII	Units
σ_{bottom}	29.168	29.165	29.163	29.157	29.150	29.124	29.117	kg m ⁻³
h	120	150	140	100	50	150	200	m
g'	3	3	4	6	6	3	2	10 ⁻⁴ m s ⁻²
bottom depth	550	600	800	530	350	600	1200	m
distance between transects	0	80	135	170	25	65	25	km
W	20	80	40	15	15	30	20	km
u_2 (LIW)	12	5	3.2*	18	53	11	7	cm s ⁻¹
u_3 (EMDW)	13	8	5*	14	46	15	17	cm s ⁻¹
ϕ (EMDW)	0.23	0.26	0.20	0.23	0.32	0.35	0.34	Sv
$F_r = \frac{ u - u_2 }{\sqrt{g' h}}$	0.1	0.2	0.1	0.2	0.8	0.2	0.5	
E^*	/	~ 0	10 ⁻⁵	10 ⁻⁴	2×10 ⁻⁴	9×10 ⁻⁴	3×10 ⁻⁴	

610

611 **Table 1.** Main experimental quantities measured by A01 in the Sicily Channel and in the Southern
612 Tyrrhenian Sea during the MATER II cruise (Figs. 1 and 3). Here σ_{bottom} is the maximum σ_θ observed
613 in the hydrographic casts; h is the bottom layer thickness; g' the reduced gravity; ϕ (EMDW) is the
614 EMDW volume transport; the Froude number is F_r ; the entrainment parameter E^* is the one computed
615 by Baringer and Price (1997b). *LIW and EMDW velocities for section III were obtained from current
616 meter measurements. Velocities for the sections were obtained by using continuity, considering the
617 total transport and dividing by the cross-sectional area

618

619

Transect	I	III	IIIa	IV	V	VII	Units
σ_{bottom}	29.167	29.165	29.163	29.156	29.148	29.119	kg m ⁻³
h	75	125	100	50	25	130	m
g'	8.3	8.2	8	7.8	7.4	6	10 ⁻⁴ m s ⁻²
bottom depth	550	700	650	500	360	1150	m
distance between transects		155	170	60	25	90	Km
W	15	5	22	15	8	18	Km
u_2 (LIW)	10	2	12	13	35	5	cm s ⁻¹
u_3 (EMDW)	12	6	3	8	27	8	cm s ⁻¹
ϕ (EMDW)	5	5.4	7.2	8	10	12	10 ⁻² Sv
$F_r = \frac{ u - u_2 }{\sqrt{g'h}}$	0.1	0.05	0.3	0.2	0.6	0.03	
E^*	2x10 ⁻⁵	10 ⁻⁵	1.3x10 ⁻⁴	4x10 ⁻⁴	4.5x10 ⁻⁴	3x10 ⁻⁴	

620

621 **Table 2.** As Table I, but for the MATER IV cruise (Fig. 1 and 4).

622

623

624

625

626

627

Figure Captions

628

629

630 **Figure 1a.** General map of the Sicily Channel: the channel length is ~ 500 km, with two sills at its
631 eastern and western entrances (~ 550 and ~ 350 m deep, respectively). Dots indicate the hydrographic
632 stations of all cross-section vertical transects; triangles indicate the position of current-meter chains.
633 The Ionian Sea is on the southeastern side of the map. From Astraldi et al. (2001).

634

635 **Figure 1b.** Main routes of the principal water masses flowing through the region: LIW (Levantine
636 Intermediate Water, dashed line), EMDW (Eastern Mediterranean Deep Water, solid line), and MAW
637 (Modified Atlantic Water, bold line). The trajectory of the EMDW corresponds to the centerline of the
638 vein in the different hydrographic sections. After Astraldi et al. (2001).

639

640 **Figure 2.** (a) Schematic representation of the three layers in a cross-flow vertical transect. The
641 interface are at $z = h_1$ for the air–sea surface, at $z = H_1+h_2$, and at $z = H_1+H_2+h_3$ for the lower
642 interfaces, with $H_1 = \text{const}$ and bottom depth = $H_1 + H_2 + H_3$. (b) Diagram of a bottom current also
643 showing the (x, y) and (ξ, ψ) coordinate systems. Modified from Astraldi et al. (2001).

644

645 **Figure 3.** MATER II cruise (January 1997): (a) characteristic isopycnal cross sections between MAW,
646 LIW, and EMDW. In these sections, Tunisia is on the left side. Note that, in section IV, the EMDW
647 flows only in the western passage of the cross section; interfacial slope modification is also visible in
648 section V. (b) Evolution of $\theta - S$ values of EMDW close to the bottom. From Astraldi et al. (2001).

649

650 **Figure 4.** MATER IV cruise (April–May 1998): (a) characteristic isopycnal cross sections between
651 surface Atlantic water, LIW, and EMDW. In these sections, Tunisia is on the left side. Note that, in
652 section IIIa, the EMDW flows only in the western passage of the cross section; interfacial slope
653 modification is also visible in sections IIIa, IV, and V. (b) Evolution of $\theta - S$ values of EMDW close to
654 the bottom. From Astraldi et al. (2001).

655

656 **Figure 5.** Modified spline interpolation of h_i (m) and u_i in (cm s^{-1}) along ξ (km); Roman numerals
657 indicate hydrograph transects shown in Figs. 3 and 4, for MATER II cruise and MATER IV,
658 respectively. The black arrows at the top show the position of the sill. Diamonds represent the cross-
659 sectional maximum velocities as obtained by the Sannino et al. (2009) numerical model (see text).

660

661 **Figure 6.** Analytic profiles for ζ (s⁻¹) and Π (m⁻¹ s⁻¹) along ξ (km) as obtained from Eqs. (13) and (15),
662 respectively. The dashed lines indicate approximate solutions for $\zeta \ll f$ and $\frac{1}{h}E(u-u_2) \approx 0$, i.e., Eq.
663 (13b). Position of the transects is also shown (see Figs. 3 and 4) for MATER II and MATER IV cruises.
664 The arrows show the position of the sill.

665
666 **Figure 7.** Analytic profile for the various terms in Eq. (18) along ξ (m), namely the friction term (bold
667 line), the PV-advection term (dots line), and the entrainment term (thin line). Position of the transects
668 is shown in Figs. 3 and 4, for MATER II cruise and MATER IV, respectively. The black arrow shows
669 the position of the sill.

670
671 **Figure 8.** Variations in χ^* , defined as $K^* \rightarrow K^* + \chi^*(\xi)$, along ξ (m), obtained through optimizing the
672 balance of Eq. (19).